Simultaneous OI 630 nm imaging observations of thermospheric gravity waves and associated revival of fossil depletions around midnight near the EIA crest

Authors:

1. **Navin Parihar**
   Indian Institute of Geomagnetism, Navi Mumbai, India
   e-mail: navindeparihar@gmail.com

2. **Saranya Padincharapad**
   (a) Equatorial Geophysical Research Laboratory, Indian Institute of Geomagnetism, Tirunelveli, India
   (b) Manonmaniam Sundaranar University, Tirunelveli, India
   e-mail: anuja8494@gmail.com

3. **Anand Kumar Singh**
   National Centre for Polar and Ocean Research, Goa, India
   e-mail: singhaaks@gmail.com

4. **Prasanna Mahavarkar**
   Indian Institute of Geomagnetism, Navi Mumbai, India
   e-mail: mahavarkarprasanna@gmail.com

5. **A. P. Dimri**
   Indian Institute of Geomagnetism, Navi Mumbai, India
   e-mail: apdimri@hotmail.com

Corresponding Author:
Navin Parihar, Indian Institute of Geomagnetism, Navi Mumbai, India
e-mail: navindeparihar@gmail.com

Key Words:
Airglow imaging; Midnight Irregularities/Depletions; Gravity wave seeding; Low-latitude ionosphere.

Abstract

We report the F-region airglow imaging of fossil plasma depletions around midnight that revived afresh under the persisting thermospheric gravity wave (GW) activity. An all-sky imager recorded these events in OI 630 nm imaging over Ranchi (23.3º N, 85.3º E, mlat. ~19º N), India, on 16 April 2012. Northward propagating and east-west aligned GWs (λ ~210 km, υ ~64 m/s, and τ ~0.91 h) were seen around midnight. Persisting for ~2 hours, this GW activity revived two co-existing and eastward drifting fossil depletions, DP1 and DP2. GWs-driven revival was prominently seen in depletion DP1, wherein its apex height grew from ~600 km to >800 km, and the level of intensity depletion increased from ~17% to 50%. Present study is novel in the sense that simultaneous observations of thermospheric GWs activity and associated evolution of depletion in OI 630 nm airglow imaging, and that too around local midnight, have not been reported earlier. Current understanding is that GW phase fronts aligned parallel to the geomagnetic field lines and eastward propagating are more effective in seeding Rayleigh-Taylor (RT) instability. Here, GW fronts were east-west aligned (i.e. perpendicular to the geomagnetic field lines) and propagated northward, yet they revived fossil depletions.

1. Introduction

Gravity waves (GWs) are well-known to influence the mesosphere-lower thermosphere-ionosphere (MLTI) region. GWs significantly contribute to the momentum and energy budget of the MLT region via the wave-dissipation processes (Fritts and Alexander, 2003; Holton, 1983). Apart from the dominant solar and geomagnetic inputs, GWs are the key element in some of the electrodynamical processes in the ionosphere e.g. irregularities, atmosphere-ionosphere (AI) coupling, traveling ionospheric disturbances, etc.. In the equatorial F-region, GWs modulate the ionospheric plasma into wave-like ionization structures. Under favourable conditions, these structures act as a seed to Generalized Rayleigh-Taylor (GRT) instability that generates the irregularities (Fritts et al., 2009; Huba and Joyce, 2007, 2010; Huba and Liu, 2020; Hysell et al., 1990; Kelley, 2009; Woodman, 2009). GWs are also important in the AI coupling during deep convection activity, thunderstorms, lightning, cyclones, tornadoes, transient luminous events (TLEs)/sprites initiation, tsunami, etc. (Azeem and Barlage, 2018; Maurya et al., 2022; Huba et al., 2015). GWs can also generate medium-scale traveling ionospheric disturbances (MSTIDs) (Fukushima et al., 2012; Figueiredo et al., 2018; Heale et al., 2022, and references cited therein). On the course of their propagation, GWs can also induce periodic fluctuations in the ionospheric parameters e.g. the electron density or total electron content (TEC), the F-region height, temperatures and winds, etc. (Ford et al., 2006, 2008; Klausner et al., 2009; Parihar et al., 2018; Vadas and Azeem, 2021) or airglow emission (Huba et al., 2015; Makela et al., 2011).

The crucial role of GWs in seeding the post-sunset equatorial spread-F (ESF) or plasma bubbles (EPBs) is fairly well understood (Abdu et al., 2009; Fritts et al., 2009; Huba and Joyce, 2007, 2010; Hysell et al., 1990; Kelley, 2009; Singh et al., 1997; Tsunoda, 2010; Tulasi Ram et al., 2014; Woodman, 2009). However, their role in the seeding of the midnight/post-midnight irregularities remains poorly understood, especially when the important criteria for the triggering of the GRT instability are absent (e.g., the favorable alignment of the solar terminator with the geomagnetic field lines and the pre-reversal enhancement, PRE, of the zonal electric field). Lately, Huba and Liu (2020) reported the global simulations of the ESF using the SAMI3/WACCM-X coupled model. SAMI3 is the abbreviation for '*Sami3 is Another Model of Ionosphere*' (Huba et al., 2008), and WACCM-X stands for the '*Whole Atmosphere Community Climate Model with thermosphere and ionosphere extension*' (Liu et al., 2010). For the first time, Huba and Liu's (2020) simulations demonstrated that GWs are the dominant seed mechanism and can spontaneously generate

the ESF, and that the EPBs develop self-consistently in the postsunset ionosphere. Studies by Nishioka et al. (2012) show that the GRT instability can occur near midnight under the influence of enhanced GW activity and then can lead to the growth of irregularities. MSTIDs are an important generation mechanism of post-midnight irregularities wherein the electric field perturbations associated with them acts as the seed (Miller et al., 2009; Taori et al., 2015). Otsuka (2018) have presented an elaborative review of these mechanisms. All-sky airglow imaging (ASAI) along with the radar, ionosonde, and GPS measurements have significantly contributed to our understanding of the crucial role of GWs in seeding the EPBs (Mendillo and Baumgardner, 1982; Mendillo et al., 1997; Taori et al., 2010; Yadav et al., 2017). *Spread-F Experiment (SpreadFEx)* carried out in Brazil during September-November 2005 is one such example (Fritts et al., 2009). In the Indian subcontinent, Sreeja et al. (2009) reported the GWs in OI 630 nm dayglow intensity variations that acted as a seed to the ESF irregularities.

GWs that give rise to the EPBs have usually been reported in the MLT region airglow imaging (e.g. Fritts et al., 2009; Paulino et al., 2011; Takahashi et al., 2009; Taori et al., 2013). Reports featuring them in the F-region airglow imaging are rare and limited to that of Makela et al. (2011), Paulino et al. (2016, 2018), Sau et al. (2018), and Smith et al. (2015). Makela et al. (2011) and Smith et al. (2015) reported the thermospheric imaging observations of GWs associated with tsunami and earthquake, respectively. Paulino et al. (2016, 2018) and Sau et al. (2018) presented their observations in OI 630 nm imaging from Brazil and India, respectively. However, these authors did not report any occurrence of depletions during the undergoing GW activity. We report, for the first time, simultaneous observations GWs and depletions in the F-region airglow imaging.

On the course of temporary campaign-based ASAI observations of OI 630 nm emission under ***Climate And Weather of Sun-Earth System (CAWSES) India Phase II Programme*** at Ranchi (23.3º N, 85.3º E, mlat. ~19º N), GW activity and "fossil depletions" were seen together on 16 April 2012 with the former reviving the latter. Fossil depletions are the remnants of airglow depletion or EPBs that have ceased growing upward or poleward; however, they continue to persist and move with ambient plasma drift. Under *Maui Middle Atmosphere and Lower Thermosphere (Maui-MALT)* initiative, Makela et al. (2004) reported their extensive observations in OI 630 nm imaging from Haleakala Volcano (20.7° N, 203.7° E; mlat. 21.3° N), Hawaii during the solar maximum of 2002-2003. Chapagain et al. (2011)

presented their limited observations from Christmas Island (2.1° N, 157.4° W, mlat. 2.8° N) during September 1995. In India, Sekar et al. (2007) presented their case study from Gadanki (13.5° N, 79.2° E, mlat. 6.3° N). However, these investigations did not discuss any resurgence of fossil depletions associated with the GW activity. Novelty of this study is that the "fossil depletions" revived into "active depletions" after the emission layer witnessed the GW activity. Lately, Wrasse et al. (2021) presented an interesting event wherein a fossil EPB merged with other ones after interacting with an electrified MSTID and turned into an active bubble.

2. Instrumentation and data

Under the ***CAWSES India Phase II Programme***, an ASAI was installed for limited nightglow observations at Ranchi (23.3º N, 85.3º E, mlat. ~19º N), located near the crest of equatorial ionization anomaly (EIA) in India during April 2012. Parihar et al. (2017) and Parihar (2019) have described this ASAI system in detail. OI 630 nm emission was monitored using a 2.2 nm half-power bandwidth optical filter having transmittance of ~77%. Our imager's field-of-view roughly covered about 7-8° latitude/longitude region at 250 km over Ranchi. Airglow images were flat-fielded to reduce the inhomogeneous contribution at lower elevations due to van Rhijn effect and non-uniform sensitivity of CCD detector at different pixels. Next, following the technique described by Wrasse et al. (2021), we detrended the individual images to enhance the contrast of airglow features using an hour running average image. Using known astral positions and assuming OI 630 nm emission peak at 250 km, the geographic coordinates of each pixel was determined following the technique of Garcia et al. (1997). Using this information, all-sky images were unwarped. We follow the technique discussed by Pimenta et al. (2003) to determine the drift velocity of depletions. First, for a given latitude, two intensity profiles along east-west direction as a function of distance was generated using two successive unwarped images. Next, the east-west displacement of depletion was estimated using these two profiles from which drift speed was determined (see Pimenta et al., 2003 for details of this technique). Similarly, the propagation characteristics of GW fronts were estimated by tracking faint crest and trough along the propagation direction in the consecutive images. As GW fronts were unclear in images, we used contrast-enhanced images. We, also, generated NS keograms to visualize GW traces and determine their speed. A keogram is a time-versus-latitude plot generated by extracting a NS column from individual images and stacking them horizontally. Next, GWs speed was, also,

estimated from the slope of wave traces seen in these keograms (Makela et al., 2006). We looked into the total electron content (TEC) measurements from an *International GNSS Service* station Hyderabad (17.3° N, 78.6° E, mlat. ~12.0° N, located nearby and south of Ranchi) to ascertain GW activity seen in the ASAI observations (Source: https://t-ict4d.ictp.it/nequick2/gnss-tec-calibration, Ciraolo et al., 2007). Quiet geomagnetic conditions prevailed on this night with $Kp < 2$, $Ap = 4$, and $-4 < Dst < 10$ *nT*.

3. Observations

Such GWs-driven revival of "fossil depletions" was recorded in airglow images during 1700-2000 UT on 16 April 2012. Here, Indian Standard Time (IST) = Universal Time (UT) + 0530 and Local Time (LT) ≈ IST. As such, 1700-2000 UT corresponds to ~1.5 h duration before and after the local midnight. Figures 1 and 2 present airglow images that depict this event seen over Ranchi during 1742-1942 UT on 16 April 2012. As the faint airglow features were getting lost in the unwarping process, warped all-sky images are presented. Supplement S1 shows the movie created from these images that feature this event. Fossil depletions of our interest that showed the GWs-driven revival are marked as **DP1** and **DP2** in Figure 1 and 2. Here, **ROI1** is the region-of-interest wherein a few weakly perceivable fronts of GWs and fossil depletions coexisted initially.

3.1 Signatures of GW activity in the F-region

We first observed faint signatures of GW activity near the southern edge of the field-of-view (FOV) during ~1715-1724 UT. Successive images showed unclear signatures of GWs activity. Starting ~1730 UT, their presence became more evident and continued until 1906 UT or so. GWs fronts were not clearly seen because of their interaction with co-existing depletions. Some weakly perceivable bright fronts are marked as 'f1', 'f2', 'f3'and 'f4' in Figure 1 and 2. Similarly, dark trough that precede fronts 'f1' and 'f2' are marked as 't1' and 't2', respectively. Often GWs in OI 630 nm imaging are faint and unclear. Under similar situations, Makela et al. (2011) found that time difference (TD) images have proven ability to reflect such GWs faint fronts. In their work, initial analysis of raw images did not show any GWs activity linked with tsunami; however, TD images indeed reflected associated GWs. We generated such TD images and are shown in Figure 3 which clearly show dark troughs 't1' and 't2' and GW fronts 'f1' and 'f2'. North-south (NS) keograms [shown in Figure 4 (a) and

(b)] showed a few clear alternating bright and dark intensity striations over the north, and their slope indicates that GWs propagated towards the north. We estimated GWs propagation characteristics using the slope of wave traces (marked by black arrow 'b1', 'b2', 'b3', 'b4') in keograms and cross-verified them with the intensity profiling technique. We found that these GWs propagated from the south to north with the phase speed (υ) of ~64 ± 2 m/s and had the horizontal wavelength (λ) and period (τ) of ~210 ± 6 km and ~0.91 ± 0.06 h, respectively.

We further looked into the TEC measurements from IGS station Hyderabad (17.3° N, 78.6° E, mlat. ~12.0° N), India to confirm this on-going GWs activity. Figure 5 shows the TEC measurements depicting GW activity in and around Hyderabad during 1700-2000 UT on this night. Figure 5 (a) shows the scatter plots of the TEC along the trajectory of ionospheric pierce points (IPPs) for different GPS satellites during 1700-1930 UT on this night. PRN numbers of GPS satellites, along with the start time at 1700 UT, are indicated next to the corresponding IPPs trajectory. TEC variations along the NS-aligned IPPs tracks (e.g. G27 and G28) clearly show the wavelike fluctuations in the 15-20° N latitude range. The temporal evolution of the TEC for a few satellites is shown in Figure 5 (b). Of our interest is G28's TEC measurement as its IPPs trajectory lay close to the imager's ROI1 during 1700-1800 UT which showed a strong signature of GWs. By performing the periodogram analysis of the temporal and spatial variation of its TEC, we estimated the propagation characteristics of GW to be τ ~0.95 ± 0.03 h, λ ~229 ± 12 km, and υ ~67 ± 5 m/s, and is in good agreement with the ASAI observations. Further, the propagation direction of GWs seen in airglow imaging is in good agreement with these previous reports. Studies on the GW activity at the MLT heights over a farther low-latitude station Prayagraj (25.5° N, formerly Allahabad) in India showed their propagation either northward or northeast around midnight during April-May (Mukherjee et al., 2010). A comprehensive study of thermospheric GWs in the ASAI observations over Tirunelveli (8.7° N) in India during 2013-2015 indicated their propagation toward the north-northwest during the equinoxes (Sau et al., 2018).

3.2 GWs-driven revival of fossil depletions

During 1730-1748 UT, faint signatures of depletion DP1 that revived were seen in the ROI1. Depletion DP1 lacked any poleward growth during 1730-1806 UT. Using the equation given in Kelley (2009) and by tracking the poleward tip of depletion, we estimated the apex height of the associated geomagnetic flux tubes (A_H) and found it to be steady at ~600 km. Within it,

the level of intensity reduction with respect to that of the ambient region (i.e., $\Delta I/I_{ambient\ region}$) was ~17 %. However, depletion DP1 drifted gradually to the east with a speed of 59-70 m/s. Beginning 1812-1818 UT, this depletion started to intensify steadily, gain contrast against the background and become noticeable. Southern end of depletion DP1 was fused with that of a preceding depletion OD2. A few faint NS-aligned depletions were also present in the ROI1. Along with depletion DP1, they intersected the EW-aligned fronts 'f1' and 'f2' of GWs, and fragmented them into few isolated structures. Later on, these structures got attached to the west wall of depletion DP1 and started moving in unison. Clear signs of two such fragments (marked as S1 and S2 in Figure 1 and 2) can be seen at ~1830 UT and ~1806-1812 UT, respectively. Starting 1824-1830 UT, we noted airglow enhancement to occur near its east wall that then started to become distinct. As a result, an *inverted arrowhead*-shaped depletion with an unusually wide southern fraction was evident during 1836-1854 UT. As two attached structures S1 and S2 drifted along with depletion DP1, they tilted considerably to the east by ~60-75° (see the ASAI images beginning 1830 UT in Figures 1 and 2). At ~1900 UT, the structure S1 was almost aligned and merged with the west wall of depletion DP1, which led to a fairly distinct west wall (seen as weak airglow enhancement). Airglow enhancement near both the east and west wall (marked as A1 and A2, respectively, in Figure 2) continued, and a linear NS-aligned depletion DP1 (having $A_H > 800$ km and $\Delta I/I_{ambient\ region}$ ~50 %) was seen at 1906-1912 UT. Within the next 6-12 min, the apex of structure S2 merged with airglow enhancement A2 near the west wall.

Next, some airglow enhancement occurred in the inner edge of the west wall of depletion DP1 at 1924 UT (see the region-of-interest, ROI2 in Figure 2). We interpret this as a consequence of some ambient plasma intrusion across its west wall. Later, such intrusion led to the disappearance of its southern fraction and the formation of an isolated depletion at 1942 UT. Possibly these disappearances occurred due to the filling of the EIA plasma into depletion across its western wall (see Otsuka et al., 2012). Similarly, fossil depletion DP2 also revived; however, its evolution was much simpler than that of depletion DP1.

4 Discussions

We present rare simultaneous observations of GWs activity and associated revival of fossil depletions in the F-region airglow imaging around midnight over an off-equatorial station Ranchi (located near the EIA crest) in India. Post-sunset ionospheric irregularities, in the

equatorial region, are generated by the GRT instability that sets off under the suitable combination of (i) favourable alignment of solar terminator with geomagnetic field lines; (ii) rapid height rise of the F-layer; (iii) absence of strong transequatorial wind and (iv) necessary seed perturbation (Fejer and Kelley, 1980; Kelley, 2009; Makela and Otsuka, 2012; Woodman, 2009). Stronger the height rise of the F-layer and an initial seed perturbation is, the faster the growth rate of GRT instability, which ultimately leads to the rapid evolution of the irregularities (Huba and Joyce, 2007; Huang et al., 1993; Hysell et al., 2014; Kelley et al., 1981; Krall et al., 2013; Tsunoda, 2010; Zalesak and Ossakow, 1980). GWs are well known to deform the bottom side plasma of the F-region into the wavelike ionization structures that then act as a seed to GRT instability, which, in turn, generates irregularities (Kelley et al., 1981; Hysell et al., 1990; Huba and Liu, 2020). While their role in the generation of the post-sunset irregularities is well known, our understanding is limited in the context of midnight/post-midnight irregularities. Present study features midnight fossil airglow depletions that revived due to undergoing GW activity and turned into an active depletion.

Northward propagating GWs having λ ~210 km, υ ~64 m/s, and τ ~0.91 h were recorded in 630 nm nightglow images during 1715-1906 UT. Supporting airglow observations, TEC measurements, too, showed the presence of similar GWs. Simultaneously, an eastward drifting fossil depletion DP1 (A_H ~600 km and $\Delta I/I_{ambient\ region}$, ~17 %) co-existed during 1730-1748 UT. Next, depletion DP1 and other co-existing depletions intercepted EW-aligned GW fronts and fragmented them during 1806-1824 UT. Subsequently, two such fragments viz. S1 and S2 that lay close to depletion DP1 got attached to its west wall, started drifting eastward in unison, tilted significantly to the east, and almost got aligned with the west wall. Next, depletion DP1 gradually intensified, surged polewards, and became a well-developed linear depletion (A_H > 800 km and $\Delta I/I_{ambient\ region}$ ~50 %) during 1906-1912 UT. Meanwhile, airglow enhancement continued to develop near both its walls and an uneven broadening was seen in its southern half. Next, some ambient plasma diffusion occurred near this uneven region leading to airglow enhancement in the inner edge of its west wall at 1924 UT. Such intrusion continued, its southern fraction gradually disappeared, and an isolated depletion was formed at 1942 UT. Present observations clearly indicate that “fossil depletion” DP1 revived and became an “active depletion” under the influence of co-existing GWs activity. Another succeeding depletion, DP2, too, showed a similar revival.

An important consideration in the GWs seeding of the GRT instability is the alignment of their wavefronts with the geomagnetic field lines. The current understanding is that the strength of the polarization electric field generated by the GWs greatly depends on the angle between them, and the maximum polarization occurs when their wavefront is aligned with the geomagnetic field (Huba et al., 2015; Hysell et al., 2014; Krall et al., 2013; Tulasi Ram et al., 2014; Tsunoda, 2010). Numerical simulations by Hysell et al. (2014) suggest that the GWs-induced modulations were the most severe when their fronts were aligned with the magnetic meridian. Using Communications/Navigation Outrage Forecasting System (C/NOFS) mission TEC measurements, Tulasi Ram et al. (2014) studied the characteristics of large-scale wave structure (LSWS) at the base of the F-region and their association with the EPBs occurrences in Southeast Asia and Africa. Authors found that the EPBs frequently occurred when the amplitudes of LSWS were adequately increased, and their phase fronts were geomagnetic field-aligned.

In the present study, the GWs fronts were east-west aligned (i.e., transverse to the geomagnetic field lines) and propagated northward. Yet, fossil depletions DP1 and DP2 revived and is intriguing. Meridional wind perturbations associated with GWs are known to be ineffective in the initiation and development of depletions. Present observations are in contrast with this notion and point towards another excitation mechanism rather than GRT instability, which we conjecture, is the spatial resonance mechanism for these reasons. Good matching was seen between the GWs phase speed (υ ~64-67 m/s) and the eastward drift of depletion DP1 (υ ~59-70 m/s). Horizontal Wind Model 2007 estimates also indicated the zonal thermospheric wind speed of 51-61 m/s (Drob et al., 2008). We estimated the speed at which the apex of DP1 progressed poleward and found it to be in the range of 46-56 m/s. Spatial resonance theory of GWs seeding of irregularities states that the effects of GWs perturbations are the strongest when its phase speed and the plasma drift velocity are nearly equal (Kelley et al., 1981). Under such conditions, the ionospheric plasma exerts the GW-associated forcing for a longer duration; thereby, accelerating the formation of ionization structures. As such, we conjecture that this GWs-driven revival of fossil depletions occurred via the spatial resonance mechanism. Numerical simulations by Huang and Kelley (1996) suggest that this mechanism can accelerate the formation of depletions. Possibly continuously undergoing GWs activity for 2 hours in the F-region sufficiently intensified the magnitude of

associated ionization modulations, which in turn triggered and sustained the revival of fossil depletions via the spatially resonant mechanism.

Similar event of GWs associated revival of a fossil depletion occurred around midnight on 06 March 2013 as well and is shown in Figure 6. On this night, GW activity persisted during 1530-1745 UT and concerned fossil depletion **DP3** revived during 1730-1854 UT. Typical ASAI images showing the signs of GW activity are presented in Figure 7. During 1636-1736 UT, GWs had λ ~196 ± 4 km, υ ~160 ± 4 m/s and τ ~0.34 ± 0.02 h, propagated from SW-NE, and their fronts were ~74º aligned with the geomagnetic field line. First, the southern fraction of depletion **DP3** drifted into the western edge of the FOV at 1706-1712 UT. Later, this depletion was seen as an isolated linear depletion during 1730-1736 UT confined within the ~20.1-23.2° N latitude regime with NS extension of ~480 ± 18 km. On course of its eastward drift, depletion **DP3** gradually intensified and developed both poleward and equatorward. During 1706-1800 UT, its base swiftly surged equatorward approximately from 20.2º to 17.7º N. Comparatively, its poleward growth was slower. When well-developed at 1900 UT, its NS extension was in 17-26º N latitudes (i.e. greater than 980 ± 22 km). Simultaneously, two structuring **BR1** and **BR2** developed on its east wall and an isolated depletion (**ID1**) lay on its east at ~20.5° N latitude. We found its drift speed to be in the 81-109 m/s range.

Meridional wind can influence the growth rate of GRT instability by altering the field-line integrated Pederson conductivity. Maruyama (1988) and Abdu et al. (2006) found that strong meridional winds could reduce the growth rate of RTI and suppress irregularities. Huba and Krall (2013) have reported both stabilizing and destabilizing effects of the meridional winds on RT instability. Devasia et al. (2002) found that a suitable combination of the meridional wind and F-region base height favours ESF development. In the present study, the meridional wind measurements using a Fabry-Perot interferometer, etc. were not available; hence, their possible role in the evolution of these fossil depletions could not be investigated.

We know that the electric field perturbations associated with MSTIDs can influence the growth of irregularities. Otsuka et al. (2012) and Shiokawa et al. (2015) reported the disappearance of an EPB upon interaction with MSTIDs and large-scale traveling ionospheric disturbances (LSTIDs), respectively. Authors suggested that the electric field associated with

MSTIDs/LSTIDs can move ambient plasma into the bubble across the geomagnetic field line through **E x B** drift which will result in the filling and subsequent disappearance of the depletion. Studies by Miller et al. (2009), Taori et al. (2015) and Takahashi et al. (2020) suggest that MSTIDs can directly seed EPBs. Simulation studies by Krall et al. (2011), further, indicates that the electric field associated with electrified MSTIDs can enhance the growth of EPBs. Lately, Wrasse et al. (2021) presented an interesting observations of the interaction of a fossil EPB with an electrified MSTID over 13.3° S. After interaction with the MSTID, concerned fossil EPB merged with other four EPBs, developed poleward and bifurcated. Using detrended TEC data, Takahashi et al. (2021) studied the LSWS over Latin America and found them to be effective in seeding EPBs.

5 Summary

We present, here, airglow imaging observations of fossil plasma depletions that revived afresh under the action of prolonged GW activity and became active depletions. Such simultaneous imaging of thermospheric GWs and depletions was recorded in the ASAI of OI 630 nm emission over Ranchi (mlat. ~19º N), India, on 16 April 2012. Salient features of the present study are as under:

1. First, airglow images showed EW-aligned and SN-propagating GWs (λ ~210 km, υ ~64 m/s, and τ ~0.91 h) over Ranchi during 1715-1906 UT. Similar GWs were, also, seen in TEC measurements over a lower latitude station Hyderabad.
2. A co-existing and prominent fossil depletion DP1 revived under this GW activity wherein its apex raised from 600 km to >800 km, and the level of intensity depletion increased from 17 % to 50 %. Another fossil depletion DP2, too, revived. Interestingly, GWs phase fronts were transverse to the geomagnetic field lines, yet two fossil depletions revived under their influence and became active depletions.
3. As GWs phase speed (υ ~64-67 m/s) nearly matched the eastward drift of depletion DP1 (υ ~59-70 m/s), we conjecture that the GWs-driven revival of these fossil depletions possibly occurred via the spatial resonance mechanism.
4. An uneven region of increased thickness existed on the southern half of the revived depletion DP1, wherein some airglow enhancement was seen later in the inner edge of its west wall. Possibly the gradual disappearance of its southern fraction occurred because of the intrusion of ambient plasma across the west wall.

Contrary to the current understanding, this study shows that the GWs fronts aligned perpendicular to the geomagnetic field lines can effectively grow irregularities. Present observations of the GWs-driven revival of fossil airglow depletions further contribute to our understanding of their generation mechanism around midnight.

Data Availability. Airglow data used in the present study are available through the institutional data repository (http://www.iigm.res.in/) or https://doi.org/10.5281/zenodo.8143215. Movie created from all-sky 630 nm nightglow images showing the gravity wave activity and the evolution of depletion DP1 and DP2 is available from https://doi.org/10.5281/zenodo.8358134. Calibrated TEC data is available from https://t-ict4d.ictp.it/nequick2/gnss-tec-calibration.

Author contributions. NP conceptualized the research problem and prepared the first draft. All authors contributed to the interpretation of results, discussion, and subsequent drafting of the manuscript.

Competing interests. The contact author has declared that none of the authors has any competing interests.

Acknowledgements: Funds for Airglow Research at ***Indian Institute of Geomagnetism*** are being provided by ***Department of Science and Technology (DST), Govt. of India, New Delhi***. GNSS TEC Calibrated data were downloaded from https://t-ict4d.ictp.it/nequick2/gnss-tec-calibration and ***Telecommunications/ICT for Development (T/ICT4D) Laboratory of the Abdus Salam International Centre for Theoretical Physics, Trieste, Italy*** is gratefully acknowledged. ***SP*** is grateful to ***Director, Indian Institute of Geomagnetism, Navi Mumbai*** for the award of Research Scholarship. Authors sincerely thank the Editor and Reviewers for their encouragement and critical comments.

References:

Abdu, M., Iyer, K. N., de Medeiros, R., Batista, I. S. and Sobral, J. H.: Thermospheric meridional wind control of equatorial spread F and evening prereversal electric field, Geophys. Res. Lett. 33 (7). http://dx.doi.org/10.1029/2005GL024835, 2006.

Abdu, M. A., Kherani, E. A., Batista, I. S., de Paula, E. R., Fritts, D. C., and Sobral, J. H.: Gravity wave initiation of equatorial spread F/plasma bubble irregularities based on observational data from the SpreadFEx campaign, Ann. Geophys., 27, 2607-2622. https://doi.org/10.5194/angeo-27-2607-2009, 2009.

Azeem, I., and Barlage, M.: Atmosphere-ionosphere coupling from convectively generated gravity waves. Adv. Space Res., 61(7), 1931-1941. https://doi.org/10.1016/j.asr.2017.09.029, 2018.

Ciraolo, L., Azpilicueta, F., Brunini, C., Meza, A. and Radicella, S. M.: Calibration errors on experimental slant total electron content (TEC) determined with GPS. J. Geod., 81, 111–120, https://doi.org/10.1007/s00190-006-0093-1, 2007.

Chapagain, N. P., Taylor, M. J., and Eccles, J. V.: Airglow observations and modeling of F region depletion zonal velocities over Christmas Island, J. Geophys. Res., 116, A02301, https://doi.org/10.1029/2010JA015958, 2011.

Devasia, C., Jyoti, N., Subbarao, K., Viswanathan, K., Tiwari, D. and Sridharan, R.: On the plausible linkage of thermospheric meridional winds with the equatorial spread F, J. Atmos. Sol.-Terrest. Phys. 64 (1), 1–12, http://dx.doi.org/10.1016/S1364-6826(01)00089-X, 2002.

Drob, D. P., Emmert, J. T., Crowley, G., Picone, J. M., Shepherd, G. G., Skinner, W., et al.: An empirical model of the Earth's horizontal wind fields: HWM07. J. Geophys. Res., 113, A12304, https://doi.org/10.1029/2008JA013668, 2008.

Fejer, B. G., and Kelley, M. C.: Ionospheric irregularities. Rev. Geophys., 18(2), 401-454, https://doi.org/10.1029/RG018i002p00401, 1980.

Figueiredo, C. A. O. B., Takahashi, H., Wrasse, C. M., Otsuka, Y., Shiokawa, K., & Barros, D.: Medium-scale traveling ionospheric disturbances observed by detrended total electron content maps over Brazil. Journal of Geophysical Research: Space Physics, 123, 2215–2227. https://doi.org/10.1002/2017JA025021, 2018.

Ford, E. A. K., Aruliah, A. L., Griffin, E. M., and McWhirter, I.: Thermospheric gravity waves in Fabry-Perot Interferometer measurements of the 630.0nm OI line, Ann. Geophys., 24, 555–566, https://doi.org/10.5194/angeo-24-555-2006, 2006.

Ford, E. A. K., Aruliah, A. L., Griffin, E. M., and McWhirter, I.: Statistical analysis of thermospheric gravity waves from Fabry-Perot Interferometer measurements of atomic oxygen, Ann. Geophys., 26, 29–45, https://doi.org/10.5194/angeo-26-29-2008, 2008.

Fritts, D. C., and Alexander, M. J.: Gravity wave dynamics and effects in the middle atmosphere, Rev. Geophys., 41, 1003, https://doi.org/10.1029/2001RG000106,1, 2003.

Fritts, D. C., Abdu, M. A., Batista, B. R., Batista, I. S., Batista, P. P., Buriti, R., Clemesha, B. R., Dautermann, T., de Paula, E. R., Fechine, B. J., Fejer, B. G., Gobbi, D., Haase, J., Kamalabadi, F., Kherani, E. A., Laughman, B., Lima, P. P., Liu, H.-L., Medeiros, A., Pautet, P.-D., Riggin, D. M., Rodrigues, F. S., São Sabbas, F., Sobral, J. H. A., Stamus, P., Takahashi, H., Taylor, M. J., Vadas, S. L., Vargas, F., and Wrasse, C. M.: Overview and summary of the Spread F Experiment (SpreadFEx), Ann. Geophys., 27, 2141–2155, https://doi.org/10.5194/angeo-27-2141-2009, 2009.

Fukushima, D., Shiokawa, K., Otsuka, Y., and Ogawa, T.: Observation of equatorial nighttime medium-scale traveling ionospheric disturbances in 630-nm airglow images over 7 years. J. Geophys. Res., 117, A10324. https://doi.org/10.1029/2012JA017758, 2012.

Garcia, F. J., Taylor, M. J., and Kelley, M. C.: Two-dimensional spectra analysis of mesospheric airglow image data. Appl. Opt., 36(29), 7374-7385. https://doi.org/10.1364/AO.36.007374, 1997.

485 Heale, C. J., Inchin, P. A., and Snively, J. B.: Primary versus secondary gravity wave
486 responses at F-region heights generated by a convective source, J. Geophys. Res. Space
487 Physics, 127, e2021JA029947, https://doi.org/10.1029/2021JA029947, 2022.
488
489 Huang, C.-S., Kelley, M. C., and Hysell, D. L.: Nonlinear Rayleigh-Taylor instabilities,
490 atmospheric gravity waves and equatorial spread F, J. Geophys. Res., 98(A9), 15631-15642,
491 https://doi.org/10.1029/93JA00762, 1993.
492
493 Huang, C.-S., and Kelley, M. C.: Nonlinear evolution of equatorial spread F: 1. On the role of
494 plasma instabilities and spatial resonance associated with gravity wave seeding, J. Geophys.
495 Res., 101(A1), 283-292, https://doi.org/10.1029/95JA02211, 1996.
496
497 Huba, J. D., and Joyce, G.: Equatorial spread F modeling: Multiple bifurcated structures,
498 secondary instabilities, large density 'bite-outs' and supersonic flows. Geophys. Res. Lett.,
499 34, L07105. https://doi.org/10.1029/2006GL028519, 2007.
500
501 Huba, J. D., Joyce, G., and Krall, J.: Three-dimensional equatorial spread F modeling,
502 Geophys. Res. Lett., 35, L10102. https://doi.org/10.1029/2008GL033509, 2008.
503
504 Huba, J. D., and Joyce, G.: Global modeling of equatorial plasma bubbles, Geophys. Res.
505 Lett., 37, L17104, https://doi.org/10.1029/2010GL044281, 2010.
506
507 Huba, J. D., and Krall, J.: Impact of meridional winds on equatorial spread F: Revisited,
508 Geophys. Res. Lett., 40, 1268– 1272, doi:10.1002/grl.50292, 2013.
509
510 Huba, J. D., Drob, D. P., Wu, T.-W., and Makela, J. J.: Modeling the ionospheric impact of
511 tsunami-driven gravity waves with SAMI3: Conjugate effects. Geophys. Res. Lett., 42,
512 5719–5726. https://doi.org/10.1002/2015GL064871, 2015.
513
514 Huba, J. D., and Liu, H.-L.: Global modeling of equatorial spread F with SAMI3/WACCM-
515 X. Geophys. Res. Lett., 47, e2020GL088258. https://doi.org/10.1029/2020GL088258, 2020.
516

517 Hysell, D. L., Kelley, M. C., Swartz, W. E., and Woodman, R. F.: Seeding and layering of
518 equatorial spread F by gravity waves. J. Geophys. Res., 95(A10), 17,253-17,260.
519 https://doi.org/10.1029/JA095iA10p17253, 1990.
520
521 Hysell, D. L., Jafari, R., Fritts, D. C., and Laughman, B.: Gravity wave effects on postsunset
522 equatorial F region stability, J. Geophys. Res. Space Physics, 119, 5847– 5860,
523 doi:10.1002/2014JA019990, 2014.
524
525 Kelley, M. C., Larsen, M. F., LaHoz, C., and McClure, J. P.: Gravity wave initiation of
526 equatorial spread F: A case study, J. Geophys. Res., 86 (A11), 9087-9100,
527 https://doi.org/10.1029/JA086iA11p09087, 1981.
528
529 Kelley, M. C.: The Earth's ionosphere: Plasma physics and electrodynamics (2nd ed.).
530 Burlington, MA: Elsevier, 2009.
531
532 Klausner, V., Fagundes, P. R., Sahai, Y., Wrasse, C. M., Pillat, V. G., and Becker-Guedes, F.:
533 Observations of GW/TID oscillations in the F2 layer at low latitude during high and low solar
534 activity, geomagnetic quiet and disturbed periods, J. Geophys. Res., 114, A02313,
535 https://doi.org/10.1029/2008JA013448, 2009.
536
537 Krall, J., Huba, J. D., Ossakow, S. L., Joyce, G., Makela, J. J., Miller, E. S., and Kelley, M.
538 C.: Modeling of equatorial plasma bubbles triggered by non-equatorial traveling ionospheric
539 disturbances. Geophys. Res. Lett., 38(8), L08103. https://doi.org/10.1029/2011GL046890,
540 2011.
541
542 Krall, J., Huba, J. D., and Fritts, D. C.: On the seeding of equatorial spread F by gravity
543 waves, Geophys. Res. Lett., 40, 661-664, https://doi.org/10.1002/grl.50144, 2013.
544
545 Makela, J. J., Ledvina, B. M., Kelley, M. C. and. Kintner, P. M: Analysis of the seasonal
546 variations of equatorial plasma bubble occurrence observed from Haleakala, Hawaii, Ann.
547 Geophys., 22, 3109-3121, https://doi.org/10.5194/angeo-22-3109-2004, 2004.
548

549 Makela, J. J., Kelley, M. C., and Nicolls, M. J.: Optical observations of the development of
550 secondary instabilities on the eastern wall of an equatorial plasma bubble. J. Geophys. Res.,
551 111, A09311, https://doi.org/10.1029/2006JA011646, 2006.
552
553 Makela, J. J., Lognonne, P., Hebert, H., Gehrels, T., Rolland, L., Allgeyer, S., et al.: Imaging
554 and modeling the ionospheric airglow response over Hawaii to the tsunami generated by the
555 Tohoku earthquake of 11 March 2011. Geophys. Res. Lett., 38, L00G02.
556 https://doi.org/10.1029/2011GL047860, 2011.
557
558 Makela, J. J., and Otsuka, Y.: Overview of nighttime ionospheric instabilities at low- and
559 mid-latitudes: Coupling aspects resulting in structuring at the mesoscale. Space Sci. Rev.,
560 168(1-4), 419-440. https://doi.org/10.1007/s11214-011-9816-6, 2012.
561
562 Maruyama, T.: A diagnostic model for equatorial spread F: 1. Model description and
563 application to electric field and neutral wind effects, J. Geophys. Res., 93 (A12), 14611–
564 14622. http://dx.doi.org/10.1029/JA093iA12p14611, 1988.
565
566 Maurya, A. K., Parihar, N., Dube, A., Singh, R., Kumar, S., Chanrion, O., Tomicic, M., and
567 Neubert, T.: Rare observations of sprites and gravity waves supporting D, E, F-regions
568 ionospheric coupling, Sci. Rep., 12, 581. https://doi.org/10.1038/s41598-021-03808-5, 2022.
569
570 Mendillo, M., and Baumgardner, J.: Airglow characteristics of equatorial plasma depletions.
571 J. Geophys. Res., 87, 7641-7652, https://doi.org/10.1029/JA087iA09p07641, 1982.
572
573 Mendillo, M., Baumgardner, J., Colerico, M., and Nottingham, D.: Imaging science
574 contributions to equatorial aeronomy: initial results from the MISETA program, J. Atmos.
575 Terr. Phys., 59, 1587-1599, https://doi.org/10.1016/S1364-6826(96)00158-7, 1997.
576
577 Miller, E. S., Makela, J. J., and Kelley, M. C.: Seeding of equatorial plasma depletions by
578 polarization electric fields from middle latitudes: Experimental evidence, Geophys. Res.
579 Lett., 36, L18105, https://doi.org/10.1029/2009GL039695, 2009.
580

Mukherjee, G. K., Pragati Shikha, R., Parihar, N., Ghodpage, R. and Patil, P. T.: Studies of the wind filtering effect of gravity waves observed at Allahabad (25.45° N, 81.85° E). Earth Planets Space 62, 309-318, https://doi.org/10.5047/eps.2009.11.008, 2010.

Nishioka, M., Otsuka, Y., Shiokawa, K., Tsugawa, T., Effendy, , Supnithi, P., Nagatsuma, T., and Murata, K. T.: On post-midnight field-aligned irregularities observed with a 30.8-MHz radar at a low latitude: Comparison with F-layer altitude near the geomagnetic equator, J. Geophys. Res., 117, A08337, https://doi.org/10.1029/2012JA017692, 2012.

Otsuka, Y., Shiokawa, K. and Ogawa, T.: Disappearance of equatorial plasma bubble after interaction with mid-latitude medium-scale traveling ionospheric disturbance, Geophysical Research Letters, 39, L14105, https://doi.org/10.1029/2012GL052286, 2012.

Otsuka, Y.: Review of the generation mechanisms of post-midnight irregularities in the equatorial and low-latitude ionosphere. Prog.. Earth Planet. Sci. 5, 57. https://doi.org/10.1186/s40645-018-0212-7, 2018.

Parihar, N., Singh, D., and Gurubaran, S.: A comparison of ground-based hydroxyl airglow temperatures with SABER/TIMED measurements over 23° N, India, Ann. Geophys., 35, 353–363, https://doi.org/10.5194/angeo-35-353-2017, 2017.

Parihar, N., Radicella, S. M., Nava, B., Migoya-Orue, Y. O., Tiwari, P., and Singh, R.: An investigation of the ionospheric F region near the EIA crest in India using OI 777.4 and 630.0 nm nightglow observations. Ann. Geophys., 36(3), 809-823. https://doi.org/10.5194/angeo-36-809-2018, 2018.

Parihar, N.: Rare occurrence of off-equatorial edge initiating and equatorward surging plasma depletions observed in OI 630-nm imaging. J. Geophys. Res. Space Physics, 124, 2887-2896. https://doi.org/10.1029/2018JA026155, 2019.

Paulino, I., Takahashi, H., Medeiros, A. F., Wrasse, C. M., Buriti, R. A., Sobral, J. H. A., and Gobbi, D.: Mesospheric gravity waves and ionospheric plasma bubbles observed during the COPEX campaign. J. Atmos. Sol.-Terr. Phys., 73(11-12), 1575-1580. https://doi.org/10.1016/j.jastp.2010.12.004, 2011.

615
616 Paulino, I., Medeiros, A. F., Vadas, S. L., Wrasse, C. M., Takahashi, H., Buriti, R. A., Leite,
617 D., Filgueira, S., Bageston, J. V., Sobral, J. H. A., and Gobbi, D.: Periodic waves in the lower
618 thermosphere observed by OI630 nm airglow images, Ann. Geophys., 34, 293-301,
619 https://doi.org/10.5194/angeo-34-293-2016, 2016.
620
621 Paulino, I., Moraes, J. F., Maranhão, G. L., Wrasse, C. M., Buriti, R. A., Medeiros, A. F.,
622 Paulino, A. R., Takahashi, H., Makela, J. J., Meriwether, J. W., and Campos, J. A. V.:
623 Intrinsic parameters of periodic waves observed in the OI6300 airglow layer over the
624 Brazilian equatorial region, Ann. Geophys., 36, 265–273, https://doi.org/10.5194/angeo-36-
625 265-2018, 2018.
626
627 Pimenta, A. A., Fagundes, P. R., Sahai, Y., Bittencourt, J. A., and Abalde, J. R.: Equatorial F-
628 region plasma depletion drifts: latitudinal and seasonal variations. Ann. Geophys., 21, 2315-
629 2322, https://doi.org/10.5194/angeo-21-2315-2003, 2003.
630
631 Sau, S., Narayanan, V. L., Gurubaran, S., and Emperumal, K.: Study of wave signatures
632 observed in thermospheric airglow imaging over the dip equatorial region. Adv. Space Res.,
633 62(7), 1762–1774, https://doi.org/10.1016/j.asr.2018.06.039, 2018.
634
635 Sekar, R., Chakrabarty, D., Sarkhel, S., Patra, A. K., Devasia, C. V., and Kelley, M. C.:
636 Identification of active fossil bubbles based on coordinated VHF radar and airglow
637 measurements, Ann. Geophys., 25, 2099-2102, https://doi.org/10.5194/angeo-25-2099-2007,
638 2007.
639
640 Shiokawa, K., Otsuka, Y., Lynn, K. J., Wilkinson, P., and Tsugawa, T.: Airglow-imaging
641 observation of plasma bubble disappearance at geomagnetically conjugate points. Earth
642 Planets and Space, 67(1), 43, https://doi.org/10.1186/s40623-015-0202-6, 2015.
643
644 Singh, S., Johnson, F. S., and Power, R. A.: Gravity wave seeding of equatorial plasma
645 bubbles. J. Geophys. Res., 102(A4), 7399– 7410, https://doi.org/10.1029/96JA03998, 1997.
646
647 Smith, S. M., Martinis, C. R., Baumgardner, J., and Mendillo, M.: All-sky imaging of
648 transglobal thermospheric gravity waves generated by the March 2011 Tohoku Earthquake, J.

649 Geophys. Res. Space Physics, 120, 10,992-10,999, https://doi.org/10.1002/2015JA021638,
650 2015.
651
652 Sreeja, V., Vineeth, C., Pant, T. K., Ravindran, S. and Sridharan, R.: Role of gravity wavelike
653 seed perturbations on the triggering of ESF-First results from unique dayglow observations,
654 Ann. Geophys., 27, 313-318, https://doi.org/10.5194/angeo-27-313-2009, 2009.
655
656 Takahashi, H., Taylor, M. J., Pautet, P.-D., Medeiros, A. F., Gobbi, D., Wrasse, C. M.,
657 Fechine, J., Abdu, M. A., Batista, I. S., Paula, E., Sobral, J. H. A., Arruda, D., Vadas, S. L.,
658 Sabbas, F. S., and Fritts, D. C.: Simultaneous observation of ionospheric plasma bubbles and
659 mesospheric gravity waves during the SpreadFEx Campaign, Ann. Geophys., 27, 1477-1487,
660 https://doi.org/10.5194/angeo-27-1477-2009, 2009.
661
662 Takahashi, H., Wrasse, C. M., Figueiredo, C. A. O. B., Barros, D., Paulino, I., Essien, P., et
663 al.: Equatorial plasma bubble occurrence under propagation of MSTID and MLT gravity
664 waves. J. Geophys. Res.: Space Physics, 125, e2019JA027566.
665 https://doi.org/10.1029/2019JA027566, 2020.
666
667 Takahashi, H., Essien, P., Figueiredo, C. A. O. B., Wrasse, C. M., Barros, D., Abdu, M. A.,
668 Otsuka, Y., Shiokawa, K., and Li, G. Z.: Multi-instrument study of longitudinal wave
669 structures for plasma bubble seeding in the equatorial ionosphere. Earth Planet. Phys., 5(5),
670 368–377. https://doi.org/10.26464/epp2021047, 2021.
671
672 Taori, A., Makela, J. J., and Taylor, M. J.: Mesospheric wave signatures and equatorial
673 plasma bubbles: A case study, J. Geophys. Res., 115, A6, A06302,
674 https://doi.org/10.1029/2009JA015088, 2010.
675
676 Taori, A., Jayaraman, A., and Kamalakar, V.: Imaging of mesosphereñthermosphere airglow
677 emissions over Gadanki (13.5° N, 79.2° E): First results. J. Atmos. Sol.-Terr. Phys., 93, 21-
678 28. https://doi.org/10.1016/j.jastp.2012.11.007, 2013.
679
680 Taori, A., Parihar, N., Ghodpage, R., Dashora, N., Sripathi, S., Kherani, E. A., and Patil, P. T.
681 (2015). Probing the possible trigger mechanisms of an equatorial plasma bubble event based

682 on multistation optical data. J. Geophys. Res. Space Physics, 120, 8835-8847.
683 https://doi.org/10.1002/2015JA021541.
684
685 Tsunoda, R. T.: On seeding equatorial spread F: Circular gravity waves, Geophys. Res. Lett.,
686 37, L10104, https://doi.org/10.1029/2010GL043422, 2010.
687
688 Tulasi Ram, S., Yamamoto, M., Tsunoda, R. T., Chau, H. D., Hoang, T. L., Damtie, B.,
689 Wassaie, M., Yatini, C. Y., Manik, T., and Tsugawa, T.: Characteristics of large-scale wave
690 structure observed from African and Southeast Asian longitudinal sectors, J. Geophys. Res.
691 Space Physics, 119, 2288-2297, https://doi.org/10.1002/2013JA019712, 2014.
692
693 Vadas, S. L., and Azeem, I.: Concentric secondary gravity waves in the thermosphere and
694 ionosphere over the continental United States on 25-26 march 2015 from deep convection. J.
695 Geophys. Res. Space Physics, 126, e2020JA028275. https://doi.org/10.1029/2020JA028275,
696 2021.
697
698 Wrasse, C. M., Figueiredo, C. A. O. B., Barros, D., Takahashi, H., Carrasco, A. J., Vital, L.
699 F. R., Rezende, L. C. A., Egito, F., Rosa, G. M., and Sampaio, A. H. R.: Interaction between
700 Equatorial Plasma Bubbles and a Medium-Scale Traveling Ionospheric Disturbance,
701 observed by OI 630 nm airglow imaging at Bom Jesus de Lapa, Brazil. Earth Planet. Phys.,
702 5(5), 397–406. https://doi.org/10.26464/epp2021045, 2021.
703
704 Woodman, R. F.: Spread F: An old equatorial aeronomy problem finally resolved? Ann.
705 Geophys., 27(5), 1915-1934. https://doi.org/10.5194/angeo-27-1915-2009, 2009.
706
707 Yadav, S., Sridharan, R., Sunda, S. and Pant, T. K.: Further refinements to the spatiotemporal
708 forecast model for L-band scintillation based on comparison with C/NOFS observations, J.
709 Geophys. Res. Space Physics, 122, 5643-5652, https://doi.org/10.1002/2017JA023869, 2017.
710
711 Zalesak, S., and Ossakow, S.: Nonlinear equatorial spread F: Spatially large bubbles resulting
712 from large horizontal scale initial perturbations. J. Geophys. Res., 85(A5), 2131-2142.
713 https://doi.org/10.1029/JA085iA05p02131, 1980.
714

Figure Captions

Figure 1. ASAI images during 1742-1830 UT over Ranchi (23.3º N, 85.3º E, mlat. ~19º N) on 16 April 2012. DP1 is the first fossil plasma depletion that showed GWs driven revival. Depletions OD1 and OD2 preceded depletion DP1. ROI1 is the region-of-interest wherein the south-north propagating GW activity and faint signatures of eastward drifting depletion DP1 were seen initially. Some weakly noticeable GWs fronts are 'f1', 'f2' and 'f3' (in succession). 't1' and 't2' are trough that precede fronts 'f1' and 'f2', respectively. 'S1' and 'S2' are the fractions of fronts 'f1' and 'f2', respectively, that subsequently got linked to the west wall of depletion DP1.

Figure 2. Same as Figure 1 but for 1836-1942 UT. DP2 is the second fossil depletion that showed GWs driven revival. Some noticeable GWs fronts are 'f3' and 'f4'. A1 and A2 are two arc-shaped regions of airglow enhancement near the east and west wall of depletion DP1. ROI2 is the region-of-interest wherein ambient plasma diffusion occurred across the west wall of depletions DP1.

Figure 3. Typical time difference ASAI of OI 630 nm emission over Ranchi showing GW activity during 1742–1830 UT.

Figure 4. (a)-(b) North-south (NS) keogram along 84.4° E and 85.3° E longitude generated from OI 630 nm images during 1730-1930 UT. Alternating bright and dark intensity striations (i.e. wave traces) can be seen over North. Probably depletions masked GWs features over South, and hence, these wave traces were not seen. Slope of these striations indicates towards the south-north movement of GW fronts. A few clear wave traces that were used to estimate speed of GWs are marked by black arrow as 'b1', 'b2', 'b3' and 'b4'.

Figure 5. (a) Scatter plot of the TEC along the track of IPPs for a few GPS satellites over Hyderabad (17.3° N, 78.6° E, mlat. ~12.0° N) during 1630-1930 UT on 16 April 2012. PRN numbers of GPS satellites along with the start time at 1700 UT are marked adjacent to the corresponding IPPs trajectory. G28's trajectory lay close to the south-west sector of the ASAI. Imager's field-of-view is shown by dashed quarter circle with its centre at Ranchi. (b) TEC variations of a few satellites showing the presence of GWs activity.

Figure 6. Selected ASAI images showing the revival of fossil depletion **DP3** during 1730-1854 UT on 06 March 2013 over Ranchi. **ROI3** is the region-of-interest wherein depletion **DP3** appeared sliced by an unclear thin streak of slightly enhanced airglow. **BR1** and **BR2** are two structuring that developed on its east wall.

Figure 7. Limited time difference ASAI images showing GW activity during 1530-1700 UT on 06 March 2013. Beginning 1336 UT, GW signatures were seen in airglow images; however, activity intensified during 1530-1736 UT. Some of clear GW fronts are marked as 'g1', 'h1' and 'k1'.

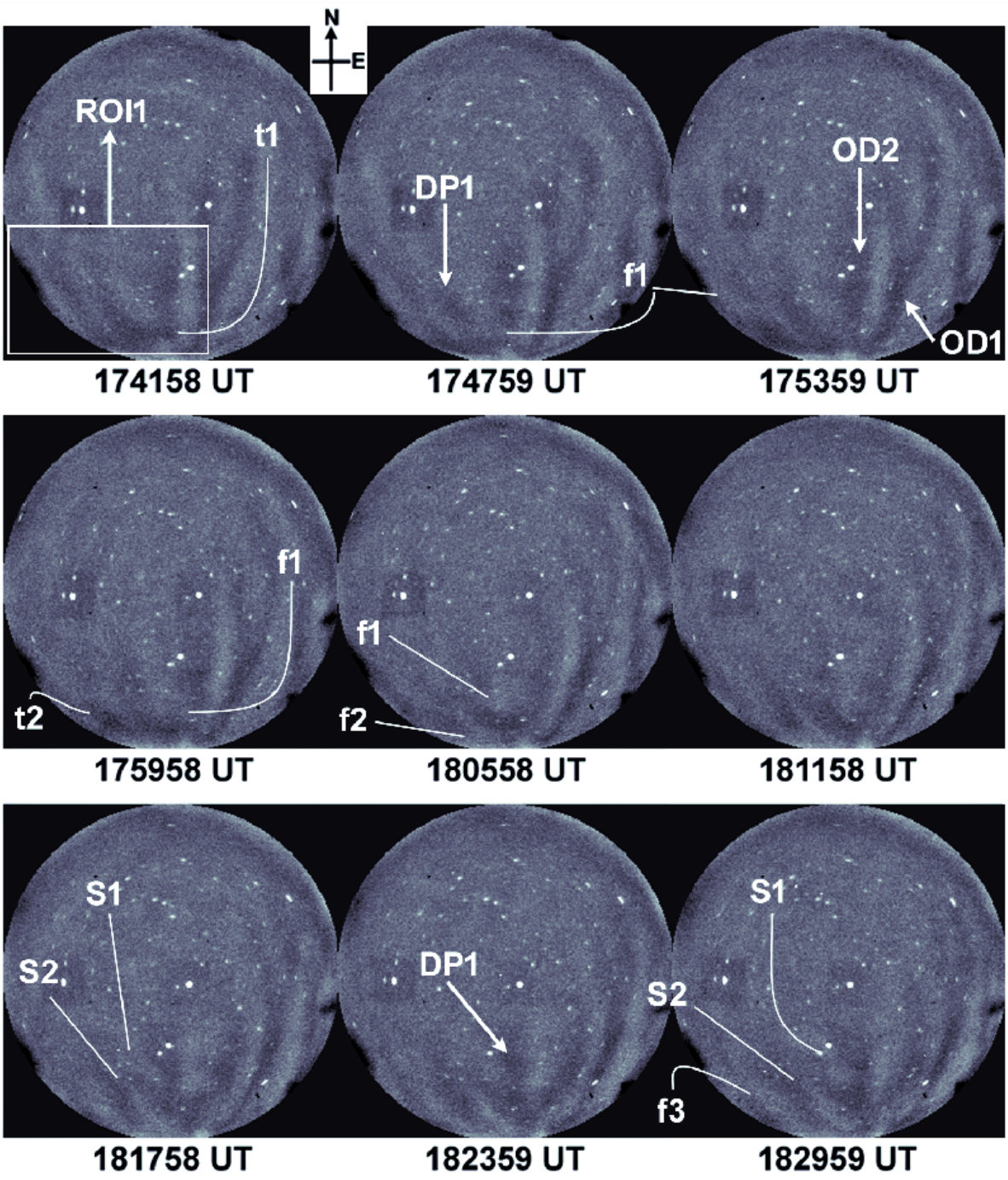

759

760 **Figure 1.** ASAI images during 1742-1830 UT over Ranchi (23.3º N, 85.3º E, mlat. ~19º N)
761 on 16 April 2012. DP1 is the first fossil plasma depletion that showed GWs driven revival.
762 Depletions OD1 and OD2 preceded depletion DP1. ROI1 is the region-of-interest wherein the
763 south-north propagating GW activity and faint signatures of eastward drifting depletion DP1
764 were seen initially. Some weakly noticeable GWs fronts are 'f1', 'f2' and 'f3' (in
765 succession). 't1' and 't2' are trough that precede fronts 'f1' and 'f2', respectively. 'S1' and
766 'S2' are the fractions of fronts 'f1' and 'f2', respectively, that subsequently got linked to the
767 west wall of depletion DP1.

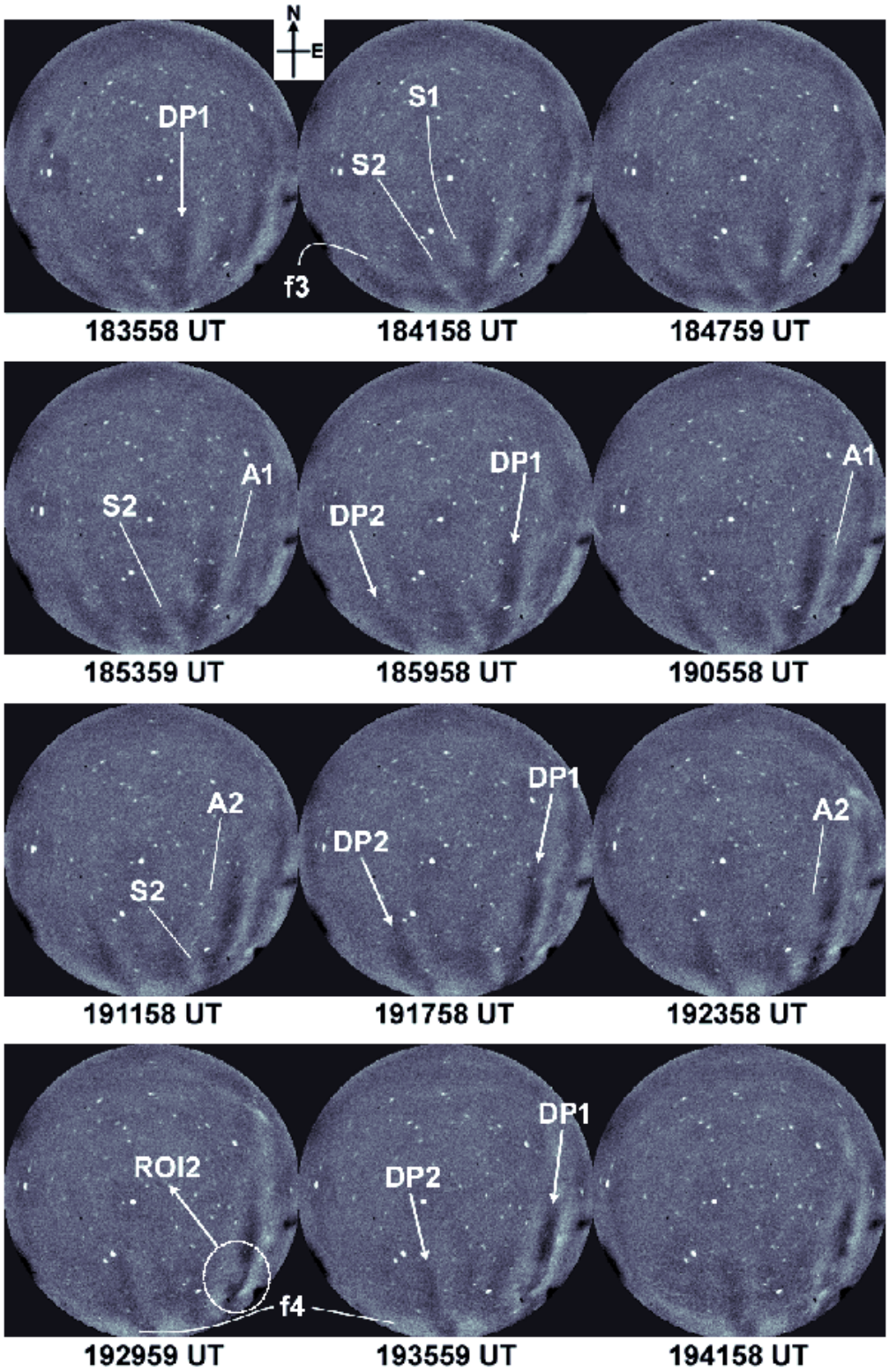

768

769 **Figure 2.** Same as Figure 1 but for 1836-1942 UT. DP2 is the second fossil depletion that
770 showed GWs driven revival. Some noticeable GWs fronts are 'f3' and 'f4'. A1 and A2 are
771 two arc-shaped regions of airglow enhancement near the east and west wall of depletion DP1.
772 ROI2 is the region-of-interest wherein ambient plasma diffusion occurred across the west
773 wall of depletions DP1.

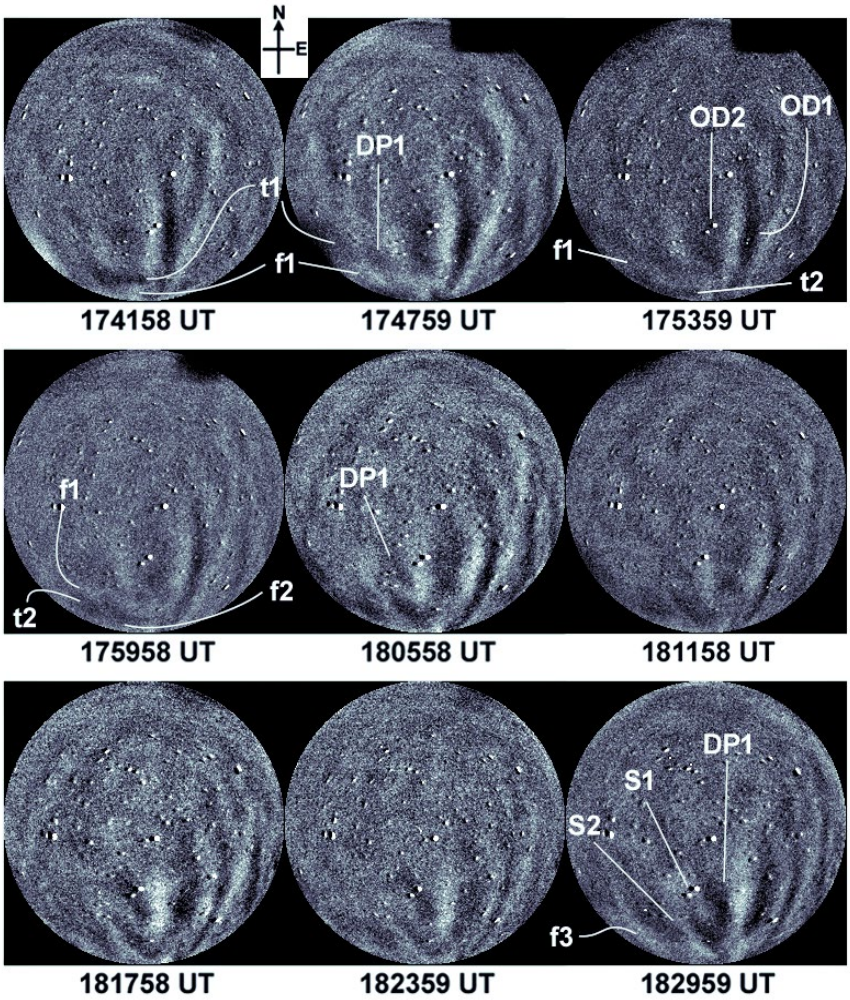

774

775 **Figure 3.** Typical time difference ASAI of OI 630 nm emission over Ranchi showing GW
776 activity during 1742–1830 UT.

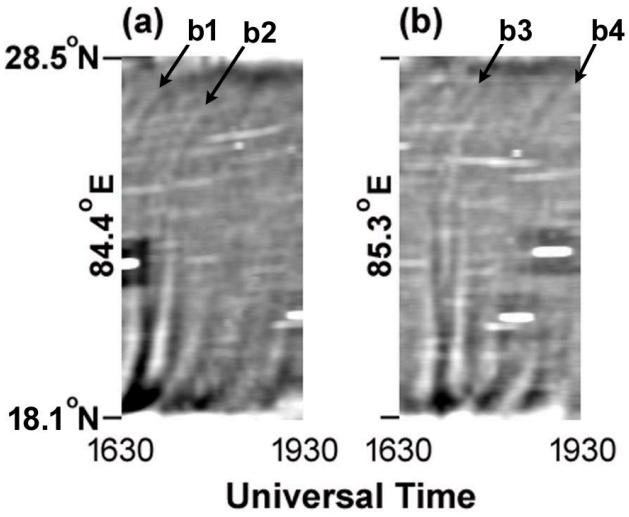

777

778 **Figure 4.** (a)-(b) North-south (NS) keogram along 84.4° E and 85.3° E longitude generated
779 from OI 630 nm images during 1730-1930 UT. Alternating bright and dark intensity
780 striations (i.e. wave traces) can be seen over North. Probably depletions masked GWs
781 features over South, and hence, these wave traces were not seen. Slope of these striations
782 indicates towards the south-north movement of GW fronts. A few clear wave traces that were
783 used to estimate speed of GWs are marked by black arrow as 'b1', 'b2', 'b3' and 'b4'.

784

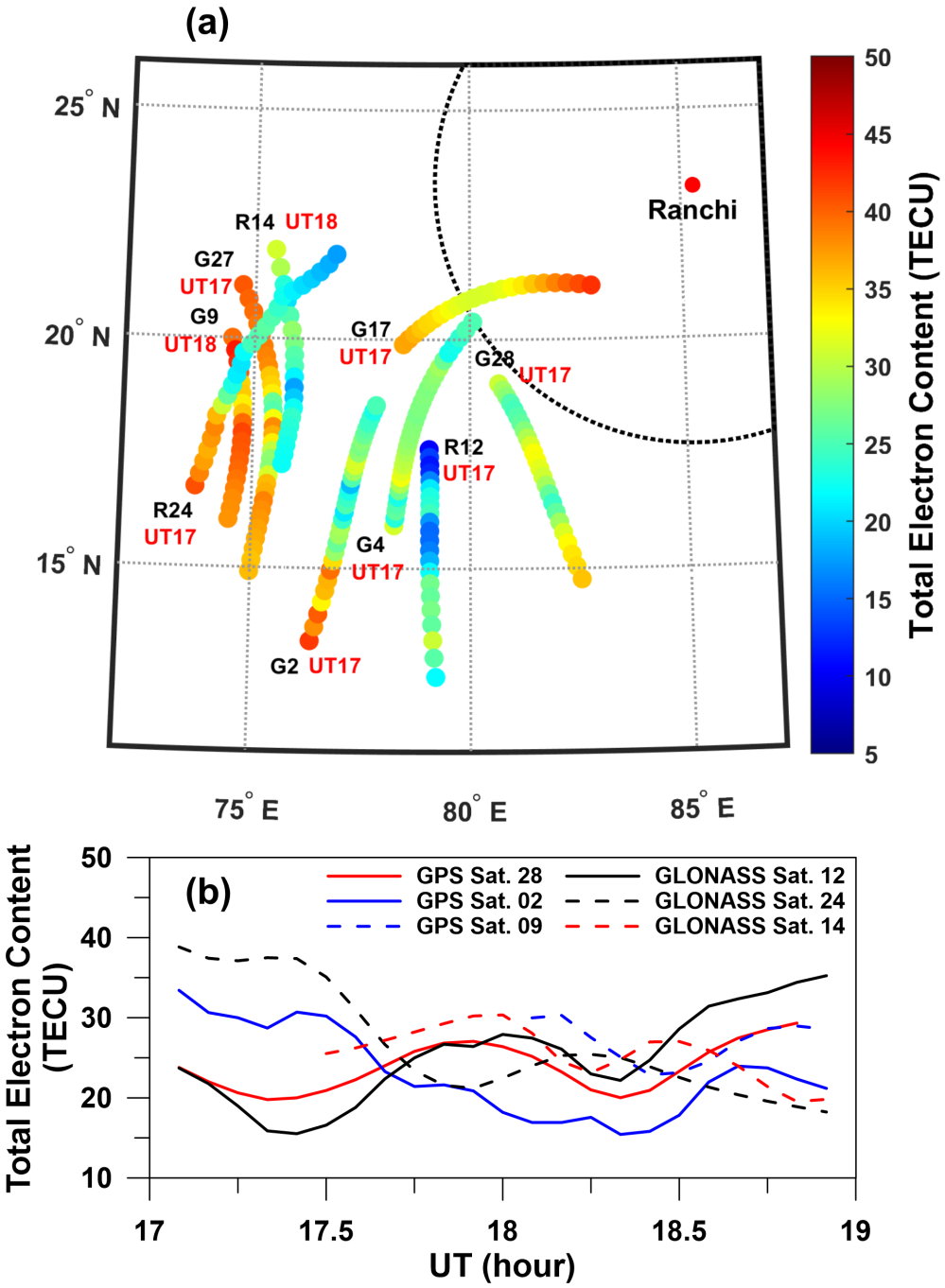

785

786 **Figure 5.** (a) Scatter plot of the TEC along the track of IPPs for a few GPS and GLONASS
787 satellites (prefixed as 'G' and 'R', respectively) in the geographic grid of 5-35° N x 65-95° E
788 during 1630-1930 UT on 16 April 2012. PRN numbers of GPS/GLONASS satellites along
789 with the start time at 1700 UT are marked adjacent to the corresponding IPPs trajectory.
790 G28's trajectory lay close to the south-west sector of the ASAI. Imager's field-of-view is
791 shown by dashed quarter circle with its centre at Ranchi. (b) TEC variations of a few
792 GPS/GLONASS satellites showing the presence of GWs activity.

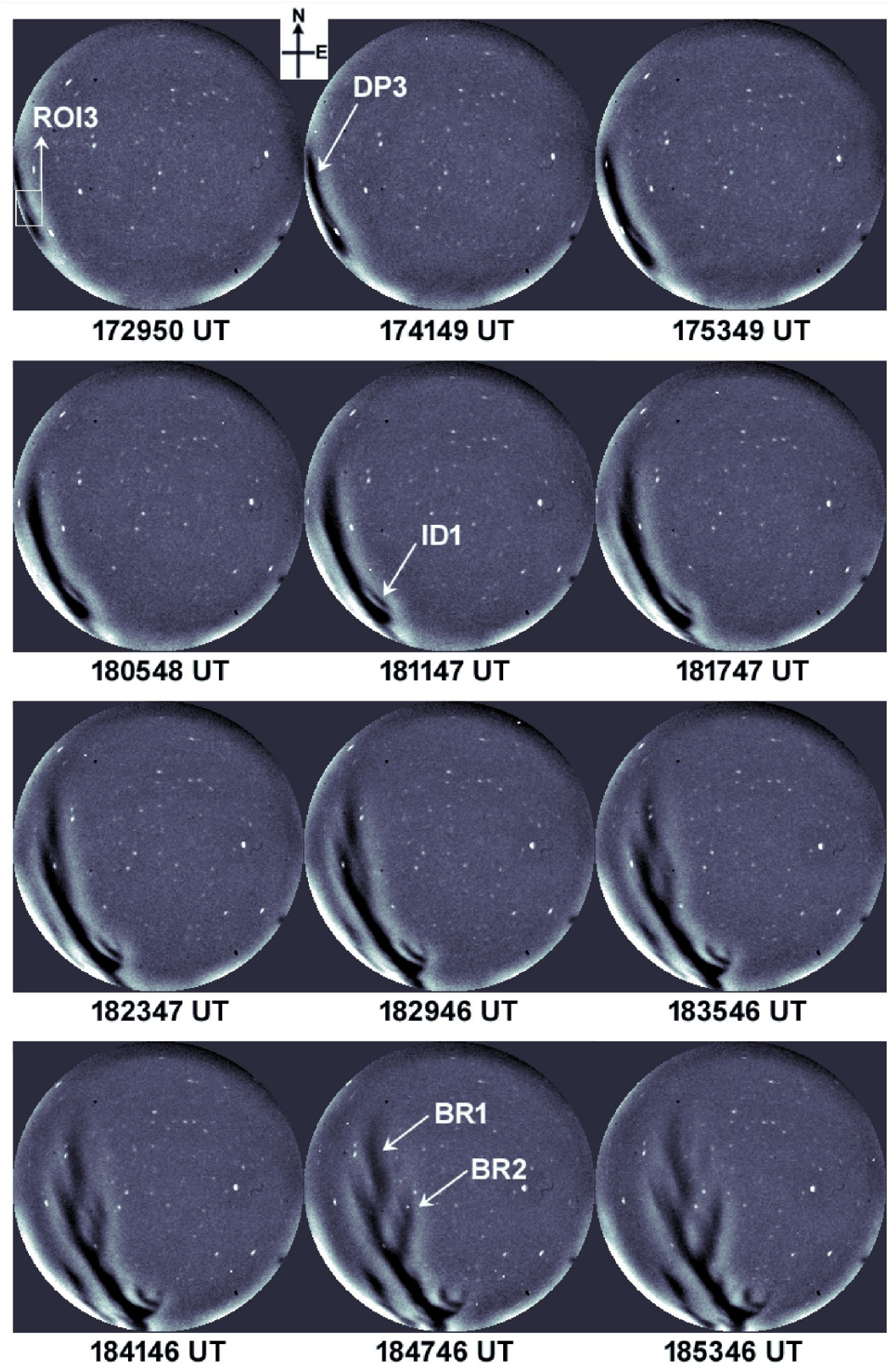

Figure 6. Selected ASAI images showing the revival of fossil depletion **DP3** during 1730-1854 UT on 06 March 2013 over Ranchi. **ROI3** is the region-of-interest wherein depletion **DP3** appeared sliced by an unclear thin streak of slightly enhanced airglow. **BR1** and **BR2** are two structuring that developed on its east wall.

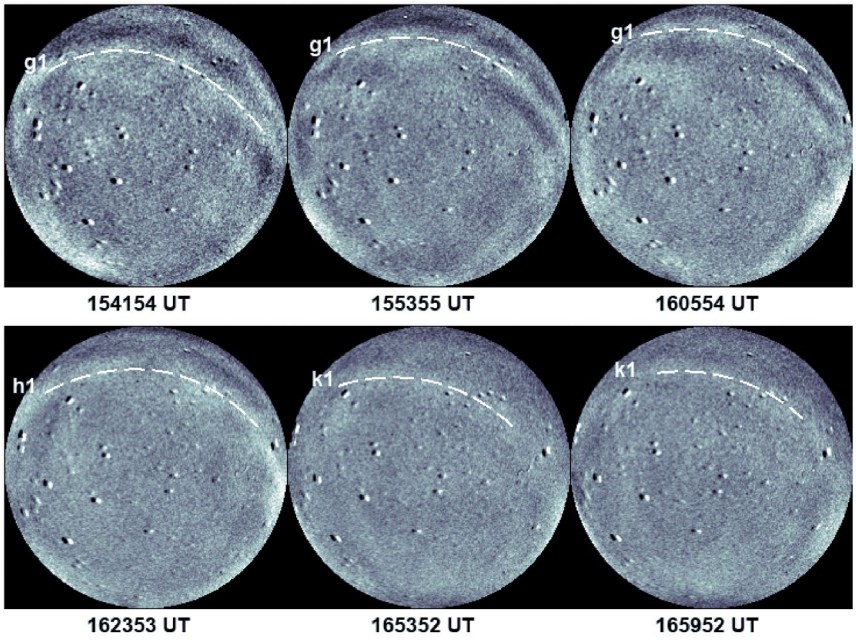

Figure 7. Limited time difference ASAI images showing GW activity during 1530-1700 UT on 06 March 2013. Beginning 1336 UT, GW signatures were seen in airglow images; however, activity intensified during 1530-1736 UT. Some of clear GW fronts are marked as 'g1', 'h1' and 'k1'.